Journal of Materials Chemistry A

ROYAL SOCIETY OF CHEMISTRY

PAPER

View Article Online
View Journal | View Issue

Cite this: J. Mater. Chem. A, 2025, 13, 38436

Photooxidation reaction kinetics of mixed-cation mixed-halide perovskite

Spencer G. Cira, Yuhuan Meng, Preetham P. Sunkari and Hugh W. Hillhouse *

In this work, we use *in situ* absorbance measurements to study the kinetics of photooxidation of a representative mixed-cation mixed-halide perovskite composition, $FA_{0.8}Cs_{0.2}Pb(I_{0.83}Br_{0.17})_3$. We identify two dominant mechanisms of degradation in the presence of oxygen: a dry photooxidation pathway (with surface reaction rate of $(0.89 \pm 0.29) \times 10^{-9}$ mol m^{-2} s^{-1} at 25 °C in dry air under 1 sun equivalent photon flux) and a water-accelerated photooxidation pathway (with a total surface reaction rate of $(1.8 \pm 0.9) \times 10^{-9}$ mol m^{-2} s^{-1} at 25 °C in 50% relative humidity air under 1 sun equivalent photon flux). Notably, water vapor is found to increase the total decomposition rate at lower temperatures but decrease the rate at higher temperatures compared to dry conditions. We propose a temperature-dependent hydrate formation pathway to explain this behavior and outline a possible degradation mechanism for both the dry and water-accelerated photooxidation pathways. A mathematical expression for the initial decomposition rate as a function of temperature, ambient partial pressures of water vapor and oxygen, and above bandgap photon flux is derived and fitted to observed rates based on the mechanistic analyses. These results provide key insights into the kinetics of decomposition for commercially relevant perovskite absorbers and may serve as a foundation for future device lifetime predictions when coupled with time-dependent mass transfer simulations.

Received 27th June 2025
Accepted 30th September 2025

DOI: 10.1039/d5ta05228a

rsc.li/materials-a

Introduction

Optoelectronic devices based on halide perovskite (HP) semiconductors are well-poised to decrease the cost of electricity generation from sunlight if their stability in the presence of oxygen and moisture can be managed by either encapsulation, gettering, or increased material stability.[1] HPs have an ABX_3 chemical formula and can be compositionally mixed at the A, B, and X sites with several organic and inorganic monovalent cations, divalent metal cations, and halides, respectively, to tailor the properties of the semiconductor. Of particular commercial interest are state-of-the-art perovskite solar cells (PSCs) which have high power conversion efficiency and low manufacturing costs using solution or vapor processing.[2,3] The tunable properties of halide perovskites enable their integration into single-junction, all-perovskite multijunction, and perovskite-on-silicon tandem solar cells. Currently, silicon photovoltaics (PV) dominate the global PV market, and perovskite-on-silicon tandem solar cells offer the possibility of incrementally increasing the efficiency of the silicon-based PV without significant increased cost of manufacturing. Thus, HPs tuned for enhanced stability and an optimal bandgap (~1.65–1.70 eV (ref. 4)) when paired with a silicon bottom cell are of the most immediate commercial interest.

Alloyed lead-based HPs ($APbX_3$) have optimized optoelectronic performance when compositionally mixed at the A-site with formamidinium ($CH(NH_2)_2^+$, FA) and cesium (Cs^+) to increase stability and performance[4] and at the X-site with bromine and iodine to tune the bandgap.[5] For X-site bromine fractions greater than ~20%, optoelectronic quality and halide phase segregation limit PSC device performance.[6–8] Thus, perovskite compositions optimized for efficient tandem architecture implementation have a ~1.65 eV bandgap (containing slightly less than 20% bromine at the X-site) which may then be made optically thin to achieve current matching in a monolithic tandem.[9] Despite the large interest in these so-called mixed-cation mixed-halide perovskites, detailed quantitative kinetic studies of the chemical reaction landscape for these materials are limited. Prior studies on FA-rich perovskites have measured the kinetics of degradation using *in situ* diffraction measurements,[10,11] *in situ* XPS,[12,13] and thermogravimetric analysis of gaseous products.[14] However, no prior works have quantitatively explored how the rate of surface reaction varies as a function of oxygen, moisture, illumination, and temperature.

In this work, we have studied the photooxidation kinetics of the perovskite $FA_{0.8}Cs_{0.2}Pb(I_{0.83}Br_{0.17})_3$, a representative composition for commercial application in tandem solar cells with a bandgap of ~1.66 eV. In previous reports on the decomposition

Department of Chemical Engineering, Clean Energy Institute, Molecular Engineering and Sciences Institute, University of Washington, Seattle, Washington 98195-1750, USA. E-mail: h2@uw.edu

of $MAPbI_3$ (ref. 15) (MA = methylammonium, $CH_3NH_3^+$) and of $FA_{0.75}Cs_{0.25}Sn_{0.5}Pb_{0.5}I_3$,[16] we used *in situ* measurements of above-bandgap optical transmittance ($\mathcal{T}$) to determine the decomposition reaction kinetics in response to environmental stressors. While the kinetic models presented in these reports help reveal the underlying chemical mechanisms responsible for perovskite decomposition and clarify the critical roles played by oxygen, water, illumination, and temperature, they have also proven valuable as predictive features in machine learning models designed to forecast the stability of perovskite materials and devices.[16–18] They may also be coupled with simulations based on the drift-diffusion equations to estimate acceleration factors and predict the performance of photovoltaic modules.[19]

Recently, we have studied the reaction kinetics of light-induced metallic lead formation in $FA_{0.8}Cs_{0.2}Pb(I_{0.83}Br_{0.17})_3$ thin films using *in situ* sub-bandgap transmittance measurements.[20] In that work, we identified that light-induced decomposition in an inert environment produces reduced lead species whereas photooxidation decomposition (which dominates at >3% ambient oxygen) produces insulating wide bandgap decomposition products. Given this critical distinction, we conduct our kinetic study on $FA_{0.8}Cs_{0.2}Pb(I_{0.83}Br_{0.17})_3$ thin films under illumination with ambient oxygen levels above 3%, where photooxidation definitively governs decomposition. Under these conditions, above bandgap absorbance measurements exclusively probe photooxidative processes, unaffected by any reduced lead species formation, thereby enabling precise, unambiguous kinetic analysis. The thin films used throughout this study were fabricated by spin-coating with an anti-solvent wash and exhibit 1 sun quasi-fermi level splitting greater than 90% of the radiative limit in addition to ambipolar diffusion length exceeding 500 nm; their optoelectronic properties and solar cell device performance have been previously reported.[20]

Here, we measure the material decomposition rate under controlled environmental conditions in which temperature, relative humidity, oxygen partial pressure, and photon flux are all controlled (refer to SI Section 1 and Fig. S1 for further discussion of this experimental setup). As a degradation experiment proceeds, we collect a transmittance measurement *in situ* (every 5 minutes). The change in absorbance with respect to time can be calculated from the following equation: $\frac{dA}{dt} = -\log_{10}\left(\frac{\mathcal{T}_{t=t}}{\mathcal{T}_{t=0}}\right)$, assuming reflectance is changing minimally relative to transmittance, which is confirmed in SI Section 2 (Fig. S2). We focus on the 'early-time' degradation because the initial absorbance decay rate provides a direct measure of material stability and correlates with the onset of material optoelectronic quality and device performance decline.[17,18] From the change in absorbance, we determine the rate of perovskite loss[15,16,20] as: $r_{\text{perovskite}} = -\frac{\rho \times \log_e 10}{M \times \alpha_0}\frac{dA}{dt}$, where ρ, M, and α_0 are the density, molecular weight, and absorption coefficient (at the probe wavelength, 630 nm in all studies presented) of the perovskite, respectively. Note that this is a 'rate of disappearance'. We conducted time series experiments (referred to as 'runs') across varied oxygen partial pressures, relative humidities, photon fluxes, and temperatures. The combined results, discussed below, inform our proposed decomposition pathways and underpin modeling of the overall decomposition rate as a function of each stressor.

Dry-photooxidation (DPO) kinetic modeling

Fig. 1 presents the time series absorbance decay and corresponding kinetic analyses for runs conducted across varied photon fluxes, oxygen concentrations (all >3%), and temperatures in humidity free environments. Fig. 1a shows the change in absorbance over time for runs under 1 sun equivalent photon flux (1.5×10^{21} photons m^{-2} s^{-1} for a 1.66 eV bandgap material) from a 540 nm monochromatic LED in dry air over a range of temperatures. In all cases, the absorbance decreases over time, indicating the loss of light absorbing perovskite material due to its degradation to wider bandgap materials (E_g > 1.97 eV/630 nm). At higher temperatures, the films exhibit a more rapid decline in absorbance. Fig. 2b presents that data in an Arrhenius plot with an observed activation energy determined from the Arrhenius fit to be 0.56 ± 0.02 eV.

For dry conditions with ambient O_2 and illumination, the most plausible reactive species driving perovskite decomposition is the superoxide radical ($O_2^{*-\bullet}$),[15,21–23] formed when an adsorbed oxygen molecule takes up a conduction band electron. From a plausible reaction mechanism based on several elementary steps (see SI Section 5 for the full derivation), we derive an expression that predicts the initial rate of perovskite loss in dry oxygen-containing environments under illumination. In this derivation, it is only necessary to assume that the elementary reaction step in which $O_2^{*-\bullet}$ reacts with the perovskite (Step (4) DPO, below) is the rate determining step (RDS) and that all other elementary reactions are in quasi-equilibrium to arrive at a mathematical expression for the dry photooxidation rate. Note that, while oxygen and/or moisture (*i.e.*, O_2^* and/or H_2O^*) induced decomposition reactions have been found to decompose FA-rich lead halide perovskites,[24,25] the decomposition rate of the films under study in the dark in both dry and 50% RH air is negligible compared to the rate under one sun (Fig. S3), consistent with prior reports.[26–28] In light of this finding, contributions from kinetically slow dark oxidation pathways are omitted in our modeling efforts throughout this manuscript. The proposed reaction pathway for DPO is the following:

$$\hbar\nu \rightleftharpoons e^- + h^+ \quad (1)$$

$$O_2 + [*] \rightleftharpoons O_2^* \quad (2)$$

$$O_2^* + e^- \rightleftharpoons O_2^{\bullet -*} \quad (3)$$

$$FA_{0.8}Cs_{0.2}Pb(I_{0.83}Br_{0.17})_3 + O_2^{\bullet -*} \rightarrow \text{degradation products} \quad (4)$$

X-ray diffraction patterns recorded during photooxidation exhibit no additional peaks over an extended period of degradation (Fig. S4), indicating the absence of detectable crystalline degradation products. It is probable that degradation products

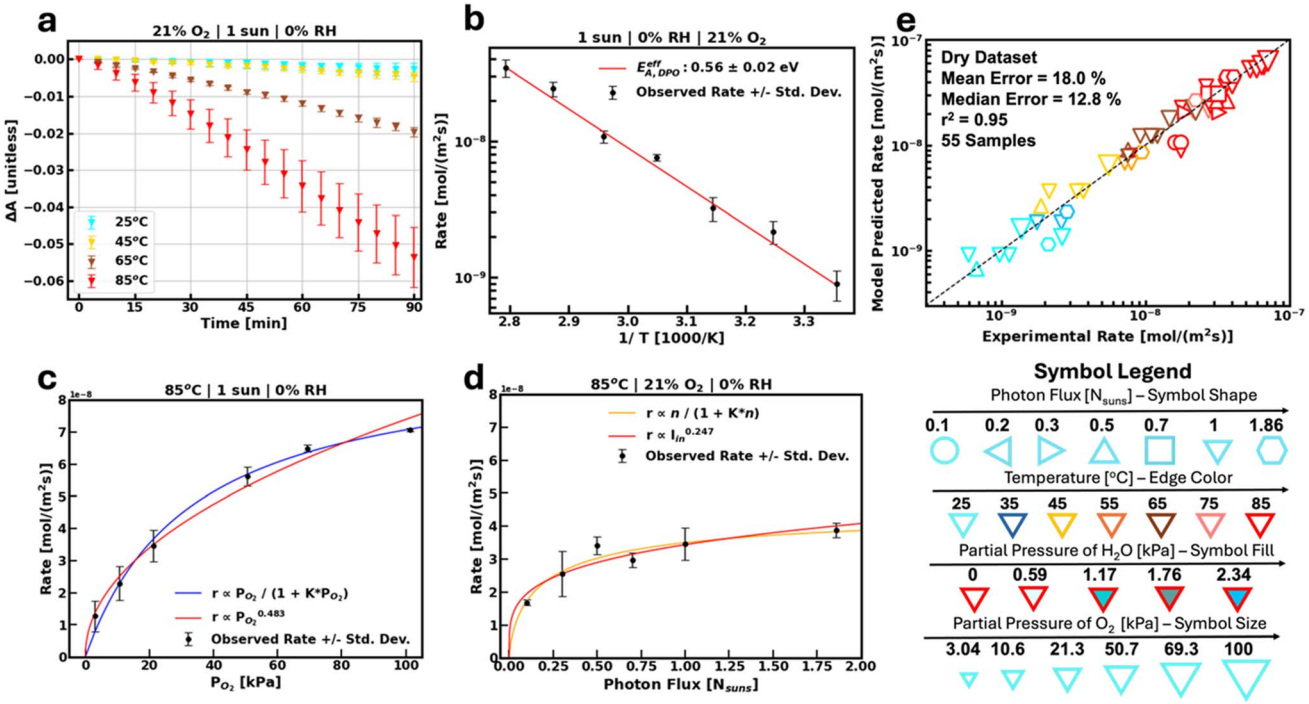

Fig. 1 Reaction kinetics for dry-photooxidation (DPO). (a) Change in absorbance over time for runs in dry air, 1 sun at 25 °C, 45 °C, 65 °C, and 85 °C. (b) Arrhenius plot for runs in dry air, 1 sun. Rate at 85 °C *versus* (c) partial pressure of O_2 and (d) photon flux with empirical power law fits (red lines) and mechanistic model fits (blue and gold lines, respectively). (e) Parity plot for the dry photooxidation model. Data includes 55 total runs in humidity free environments over a range of O_2 partial pressure, photon fluxes, and temperatures demonstrating a strong fit of the model to the data (symbol legend included below).

are a mixture of amorphous compounds including delta phase pure or mixed cation/halide perovskites,[24] lead halides (PbX_2),[29] and residual organic decomposition products.[30] Vapor phase products are likely gaseous diatomic halides (X_2)[31] and volatilized organic compounds.[30] Despite this, so long as the assumptions that Step (4) DPO is the RDS and that the products do not absorb the incident probe 630 nm light hold, the resulting rate equation for DPO is the following:

$$r_{\mathrm{DPO}} = k_{\mathrm{DPO}} \frac{P_{\mathrm{O_2}} n}{1 + K_2 P_{\mathrm{O_2}} (1 + K_3 n)} \quad (5)$$

where $k_{\mathrm{DPO}} = k_{0,\mathrm{DPO}} \exp\left(\frac{-E_{\mathrm{A,DPO}}^{\mathrm{eff}}}{k_{\mathrm{B}} T}\right)$, K_2 is the equilibrium constant associated with oxygen adsorption (Step (2) DPO), and K_3 is the equilibrium constant associated with reduction of adsorbed oxygen (Step (3) DPO).

The experimentally observed rate data at 85 °C is plotted over a range of oxygen partial pressures (no humidity) under 1 sun photon flux in Fig. 1c and over a range of photon fluxes in dry air in Fig. 1d. While empirical sublinear exponential fits to the data are quite good (red traces in Fig. 1c and d), the mechanistic models (blue and gold traces in Fig. 1c and d, respectively) deliver an even better fit, providing important insights into the fidelity of the derived mathematical form. Note that we have previously determined that the activity of photoexcited species (electrons, n, in the case of photooxidation) scales as $I_{\mathrm{in}}^{0.72}$ for this composition,[20] where I_{in} is the incident above bandgap photon flux. The mechanistic model in Fig. 1d (gold trace) is fit based on this result.

Runs at 1 sun, 21% O_2 over a range of temperatures are used to determine the effective activation energy (Fig. 1b). The entire dry dataset is used to determine the temperature independent prefactor, $k_{0,\mathrm{DPO}}$, and the two equilibrium rate constants, K_2 and K_3, *via* the non-linear least-squares method. K_2 and K_3 may have temperature dependences. However, the fit to the data is quite good over a range of temperatures, oxygen partial pressures, and illumination intensities (Fig. 1e), suggesting that associated temperature dependences are negligible over the temperature ranges in this study. Because the fitting parameters are non-linear, we applied a bootstrap procedure with 10 000 resamples (Fig. S6) to estimate parameter uncertainty.[32] In this approach, we resampled the original data with replacement, refit the model to each synthetic dataset, and derived standard deviations and 95% confidence intervals from the resulting parameter distributions. The final DPO parameter estimates and their uncertainty measures are presented in Table 1. The dry photooxidation model fits the dry dataset (55 samples) with a median error, mean error, and r^2 value of 12.8%, 18.0%, and 0.95, respectively, indicating an excellent fit of the data (Fig. 1e). Expanded details for the fitting procedure for the dry photooxidation model are included in SI Section 6.

Water-accelerated photooxidation (WPO) kinetic modeling

Having established a model for decomposition of $FA_{0.8}Cs_{0.2}Pb(I_{0.83}Br_{0.17})_3$ in dry oxygen containing environments under

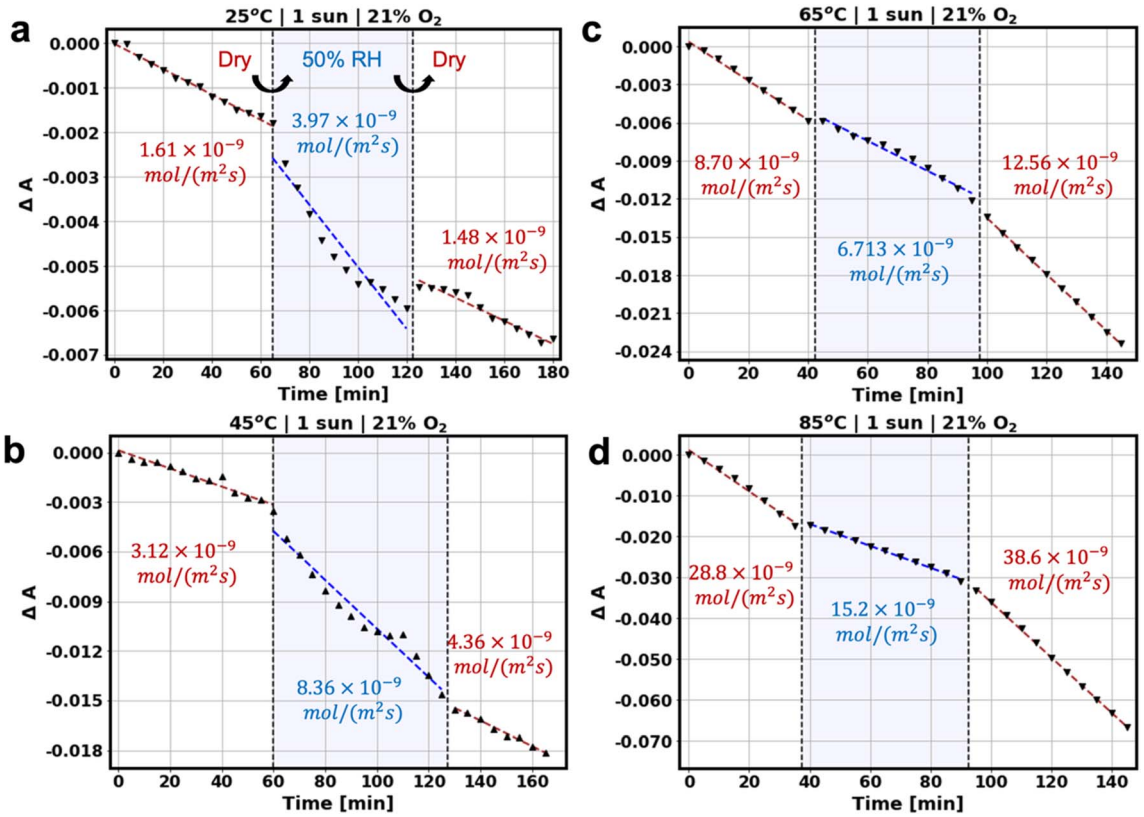

Fig. 2 Water vapor 'On–off' absorbance tracking. Degradation at 1 sun equivalent illumination in air at (a) 25 °C, (b) 45 °C, (c) 65 °C, and (d) 85 °C. Experiments start in dry air, followed by 50% RH air, and then are switched back to dry air. The calculated rate for each condition is shown in the plots. Note the difference in range of the change of absorbance for each temperature.

illumination, we next consider the influence of water on the overall degradation rate. Our previous reports identified that the introduction of water vapor to an oxygen containing atmosphere increases the net photooxidation rate of $MAPbI_3$ (ref. 15) and the net oxidation rate of $FA_{0.75}Cs_{0.25}Sn_{0.5}Pb_{0.5}I_3$.[16] This behavior is more pronounced at lower temperatures than higher temperatures (posited to be a result of lower water surface coverage at higher temperatures compared to lower temperatures). Fig. 2 shows the results of several 'on–off' experiments in which the absorbance change of the $FA_{0.8}Cs_{0.2}Pb(I_{0.83}Br_{0.17})_3$ films over the course of degradation is observed. These experiments are conducted in the same environmental chamber described in SI Section 1. Each run begins in dry air at the specified temperature. After some time, humidity is introduced into the chamber (50% RH). Finally, the gas flow is switched back to dry air. We isolate the effect that the presence of water vapor has on the overall rate by comparing the absorbance change over time in each of the three windows. The volume of the environmental chamber used is ~300 ml, and at a flow rate of 3 L min^{-1} of inlet gas, it reaches 99% of the way to its new humidity set point in <30 seconds. This rapid exchange ensures that each humidity switch is effectively instantaneous for these measurements.

Interestingly, we observe a unique phenomenon in which the effect of adding water is a net increase in perovskite decomposition rate at lower temperatures (25 °C, 45 °C, Fig. 2a and b,

Table 1 Best-fit parameters for the full kinetic photooxidation model for $FA_{0.8}Cs_{0.2}Pb(I_{0.83}Br_{0.17})_3$ thin films

Parameter	Value	Units
$k_{0,DPO}$	$(1.5 \pm 0.2) \times 10^{-16}$	mol m^{-2} s^{-1} kPa^{-1} (photons m^{-2} s^{-1})$^{-0.72}$
$E_{A,DPO}^{eff}$	0.56 ± 0.02	eV
K_2	$(9.5 \pm 1.2) \times 10^{-4}$	kPa^{-1}
K_3	$(2.3 \pm 0.4) \times 10^{-14}$	(photons m^{-2} s^{-1})$^{-0.72}$
$k_{0,WPO}$	$(1.3 \pm 0.2) \times 10^{-27}$	mol m^{-2} s^{-1} kPa^{-2} (photons m^{-2} s^{-1})$^{-0.72}$
$E_{A,WPO}^{eff}$	-0.12 ± 0.12	eV
$f_{hydrate}$	0.55	Unitless
$K_{0,hydrate}$	3.2×10^{22}	kPa^{-1}
$\Delta H_{hydrate}^{eff}$	1.5 ± 0.4	eV

respectively) and a net decrease in rate at higher temperatures (65 °C, 85 °C, Fig. 2c and d, respectively) compared to dry conditions. The associated water acceleration rate factor (50% RH rate divided by the initial dry rate) for these runs are 2.47, 2.68, 0.77, and 0.53 for the 25 °C, 45 °C, 65 °C, and 85 °C run, respectively. This counterintuitive result is confirmed with *ex situ* spectral absorption measurements (Fig. S5).

Several surface reactions are possible that may produce other reactive oxygen species (ROSs) in addition to superoxide when water vapor is also present in the ambient. These include but are not limited to reactions between superoxide and adsorbed water to form hydroxyl radicals and the further reactions to form hydrogen peroxide (both of which are strong oxidizers capable of decomposing the perovskite[33,34]). The generation of these additional, plausible ROSs may activate alternative degradation pathways that, in total, could accelerate the decomposition rate of $FA_{0.8}Cs_{0.2}Pb(I_{0.83}Br_{0.17})_3$ relative to that under dry conditions. Water may also competitively adsorb with oxygen and/or form perovskite hydrates, reducing the surface coverage of oxygen and superoxide and by extension lowering the superoxide induced decomposition rate (dry photooxidation). If competitive adsorption of water effectively displaces oxygen and superoxide from the surface, the net decomposition rate of $FA_{0.8}Cs_{0.2}Pb(I_{0.83}Br_{0.17})_3$ under humid conditions could be reduced compared to that under dry conditions. We propose that the interplay between competitive adsorption and additional ROS generation underlies the observed temperature dependent decomposition behavior. This posited explanation is further explained in the subsequent paragraphs. We note that McAndrews *et al.* reported that moisture uptake can influence stability through stress-relaxation mechanisms,[35] which we do not explore here but acknowledge as a possible contributing factor.

At lower temperatures, the exothermic water adsorption enthalpy outweighs the entropic penalty, increasing surface H_2O^* coverage relative to elevated temperatures. Adsorbed water then reacts with $O_2^{\cdot-*}$ to produce secondary ROSs such as hydroxyl radicals.[36] Hydroxyl radicals, or other secondary ROSs, open an alternative decomposition route with a lower transition-state energy barrier, yielding a reduced observed activation energy for the overall reaction.[15] Note that, in order for water to react with superoxide radicals, we assume that it must be present as unreacted adsorbed water (H_2O^*).

In contrast, at higher temperatures, there is a decrease in the net rate, implying the onset of a competing water-mediated process that suppresses the net photooxidation rate. This high-temperature slowdown motivates our proposal of a hydrated-perovskite pathway. We postulate that, in the presence of water vapor, a surface hydration reaction between pristine perovskite and gas-phase H_2O rapidly reaches quasi-equilibrium with ambient humidity (observed predominately at elevated temperatures), generating a hydrated perovskite phase. This process is fundamentally different from simple water adsorption, where an adsorbed molecule can detach and return the site to an active state. In the case of hydrate formation, vapor phase water first binds reversibly to an available site and, from this precursor state, undergoes a surface rearrangement with the perovskite lattice. This rearrangement produces a hydrate phase that annihilates the associated active site and prevents the bound water molecule from participating in further ROS-generating reactions. Only when the hydrate itself decomposes is the site restored.

It is important to note the role of site sampling dynamics in the proposed pathways. In all temperature regimes, adsorption sites are assumed to be sampled rapidly. Because both adsorption and desorption are fast, equilibrium coverage, not kinetic limitation, governs surface occupancy. At elevated temperatures, surface-bound free water (H_2O^*) coverage is low because excess thermal energy drives rapid desorption, keeping the equilibrium coverage minimal. However, the same thermal energy also enables hydrate formation at available active sites. Thus, due to rapid site sampling and the strong driving force for hydrate formation, these sites are quickly occupied, and the hydrate formation reaction proceeds.

In our model (below), we represent the hydrated species as (1) in quasi-equilibrium with gas-phase water, (2) kinetically inactive toward degradation over the experimental timescale, and (3) reversible in nature.[37–41] Functionally, an additional factor is introduced that accounts for water's effect on the total number of active adsorption sites on the perovskite surface. First-principles calculations of perovskite–water interactions show that hydrate formation likelihood depends on surface termination sites.[42] Combined experimental and theoretical studies further demonstrate that water-induced degradation varies across crystal facets.[43] To capture this surface heterogeneity, a factor that quantifies the fraction of total sites that are susceptible to hydrate formation (f_{hydrate}) is included.

The elementary reaction steps of the plausible water-accelerated photooxidation pathway can be written as the following:

$$\hbar\nu \rightleftharpoons e^- + h^+ \quad (6)$$

$$O_2 + [*] \rightleftharpoons O_2^* \quad (7)$$

$$O_2^* + e^- \rightleftharpoons O_2^{\cdot-*} \quad (8)$$

$$H_2O + [*] \rightleftharpoons H_2O^* \quad (9)$$

$$H_2O^* + O_2^{\cdot-*} \rightleftharpoons OH^- + HO_2^* \quad (10)$$

$$FA_{0.8}Cs_{0.2}Pb(I_{0.83}Br_{0.17})_3 + OH^- \rightarrow \text{degradation products} \quad (11)$$

Note that ROSs aside from OH^- may form under these conditions and contribute to decomposition; here, we choose to model the hydroxyl mediated pathway while recognizing that alternative ROS-driven routes may also operate. It is assumed that surface adsorbed water (H_2O^*) remains in the low-coverage (linear) regime of the Langmuir isotherm, allowing omission from the denominator of eqn (12) below. Using the rate-determining step approximation (Step (10) WPO) with all prior steps in quasi-equilibrium, the resulting WPO rate equation is:

$$r_{WPO} = k_{WPO}\frac{P_{O_2} n P_{H_2O}}{(1 + K_2 P_{O_2}(1 + K_3 n))^2} \quad (12)$$

where $k_{WPO} = k_{0,WPO}\exp\left(\frac{-E^{eff}_{A,WPO}}{k_B T}\right)$, and K_2 and K_3 are again equilibrium constants associated with oxygen adsorption and adsorbed oxygen reduction by conduction band electrons, respectively. The complete derivation of the WPO rate equation is included in SI Section 7.

The pathway for the hydrated perovskite formation can be written as the following:

$$H_2O + [*]_{avail} \rightleftharpoons H_2O^* \quad (13)$$

$$H_2O^* + FA_{0.8}Cs_{0.2}Pb(I_{0.83}Br_{0.17})_3 \rightleftharpoons H_2O^*\cdot FA_{0.8}Cs_{0.2}Pb(I_{0.83}Br_{0.17})_3 \quad (14)$$

An expression that captures the reduction in total surface adsorption sites ($[*]_{total}$) due to the hydrate formation (HF) pathway is presented below (eqn (15)). Because $[*]_{total}$ is contained within the prefactor of the rate equations for both the DPO and WPO pathways (SI Sections 5 and 7), it is necessary to modify both the DPO and WPO rate equations to account for relative changes in this value. A site balance on total adsorption sites, incorporating temperature-dependent equilibrium constants for hydrate formation, yields eqn (15) below. A complete derivation is provided in SI Section 8. The following equation quantifies the fraction of total available active adsorption sites relative to the total $\left(f_{active} = \frac{[*]_{available}}{[*]_{total}}\right)$:

$$f_{active} = 1 - f_{hydrate}\frac{K_{hydrate}P_{H_2O}}{1 + K_2 P_{O_2}(1 + K_3 n) + K_{hydrate}P_{H_2O}} \quad (15)$$

where $K_{hydrate}$ is a temperature dependent equilibrium constant associated with hydrate formation and is equal to $K_{0,hydrate}\exp\left(\frac{-\Delta H^{eff}_{hydrate}}{k_B T}\right)$. $f_{hydrate}$ is the fraction of total sites that are available to hydrate formation $\left(\frac{[*]_{act,water}}{[*]_{total}}\right)$. The fitting of the remaining parameters that define the WPO and HF pathways is discussed below.

From the derivations for DPO, WPO, and the hydrate formation reaction, a total rate equation for the photooxidation of $FA_{0.8}Cs_{0.2}Pb(I_{0.83}Br_{0.17})_3$ in oxygen containing environments under illumination is established. We begin by noting that the total rate is assumed to be a sum of the contributions from the dry-photooxidation and water-accelerated photooxidation pathway:

$$r_{total} = r_{DPO} + r_{WPO}$$

Including the effect that hydrate formation has on total adsorption sites, the total photooxidation reaction rate can be written as the following:

$$r_{total} = \left[k_{DPO}\frac{P_{O_2} n}{1 + K_2 P_{O_2}(1 + K_3 n)} + k_{WPO}\frac{P_{O_2} n P_{H_2O}}{(1 + K_2 P_{O_2}(1 + K_3 n))^2}\right] \times \left[1 - f_{hydrate}\frac{K_{hydrate}P_{H_2O}}{1 + K_2 P_{O_2}(1 + K_3 n) + K_{hydrate}P_{H_2O}}\right] \quad (16)$$

Fig. 3a shows the change in absorbance over time for runs in 50% RH at 25, 45, 65, and 85 °C. Reaction rates increase with temperature but less steeply than in dry air. Fig. 3b is an Arrhenius plot in which runs at 100% RH (dark blue) and 50% RH (light blue) are compared to the dry-photooxidation model. At low temperatures (25–45 °C), we observe a decrease in the apparent activation energy with an increase in relative humidity. The magnitude of the observed rate is also higher than the dry-photooxidation rate. These two results are commensurate with our initial hypothesis of an additional water-accelerated photooxidation pathway that occurs predominately at lower temperatures. Consistent with prior results on other perovskite compositions, this pathway exhibits a negative effective activation energy because of the substantial enthalpy of water adsorption.[15,16] However, at high temperatures (45–85 °C), the apparent activation energy is nearly identical for runs at 50% RH and 100% RH. This observation supports the hydrate formation hypothesis but also indicates that available hydrate formation sites are becoming saturated, with the surface coverage term approaching unity under these conditions. Fig. 3c is a plot of the rate of disappearance of perovskite *versus* the partial pressure of water vapor for runs at 85 °C under 1 sun in air. Here, the rate is accounted for almost entirely by reactions precipitated by the formation of superoxide radical ($[H_2O^*]$ is expected to be very low while $[H_2O^*\cdot FA_{0.8}Cs_{0.2}Pb(I_{0.83}Br_{0.17})_3]$ is expected to be appreciable at this temperature). We model the rate (the red line) as the dry-photooxidation rate at 85 °C in dry air under 1 sun multiplied by the hydrate formation factor (eqn (15)). This fit provides an estimate for the fraction of total adsorption sites available for hydrate formation ($f_{hydrate} = 0.55$) in addition to a reference equilibrium constant for hydrate formation ($K_{hydrate}$ ($T = 85$ °C) $= 47$ kPa^{-1}).

To fit the remaining parameters ($E^{eff}_{A,WPO}$, $\Delta H^{eff}_{hydrate}$, $k_{0,WPO}$) that define the total rate (eqn (16)), we divided the 65-sample humid dataset into multiple subsets defined by distinct temperature ranges and performed a grid search optimization.[44] This exhaustive search is necessary because activation energies appear in the exponent of the Arrhenius term, making gradient-based methods extremely sensitive to initial guesses and prone to failure unless seeded very close to the true values. The grid search involves selecting pairs of $E^{eff}_{A,WPO}$ and $\Delta H^{eff}_{hydrate}$ values over a broad range and fitting $k_{0,WPO}$ to optimize the fit. The results of these grid searches are presented in SI Section 9 and Fig. S7. The most optimal parameters based on a minimization of the sum of squared residuals are when $E^{eff}_{A,WPO}$ and $\Delta H^{eff}_{hydrate}$ are equal to −0.12 eV and 1.48 eV, respectively. In agreement with our prior work, we find that a negative effective activation energy associated with WPO

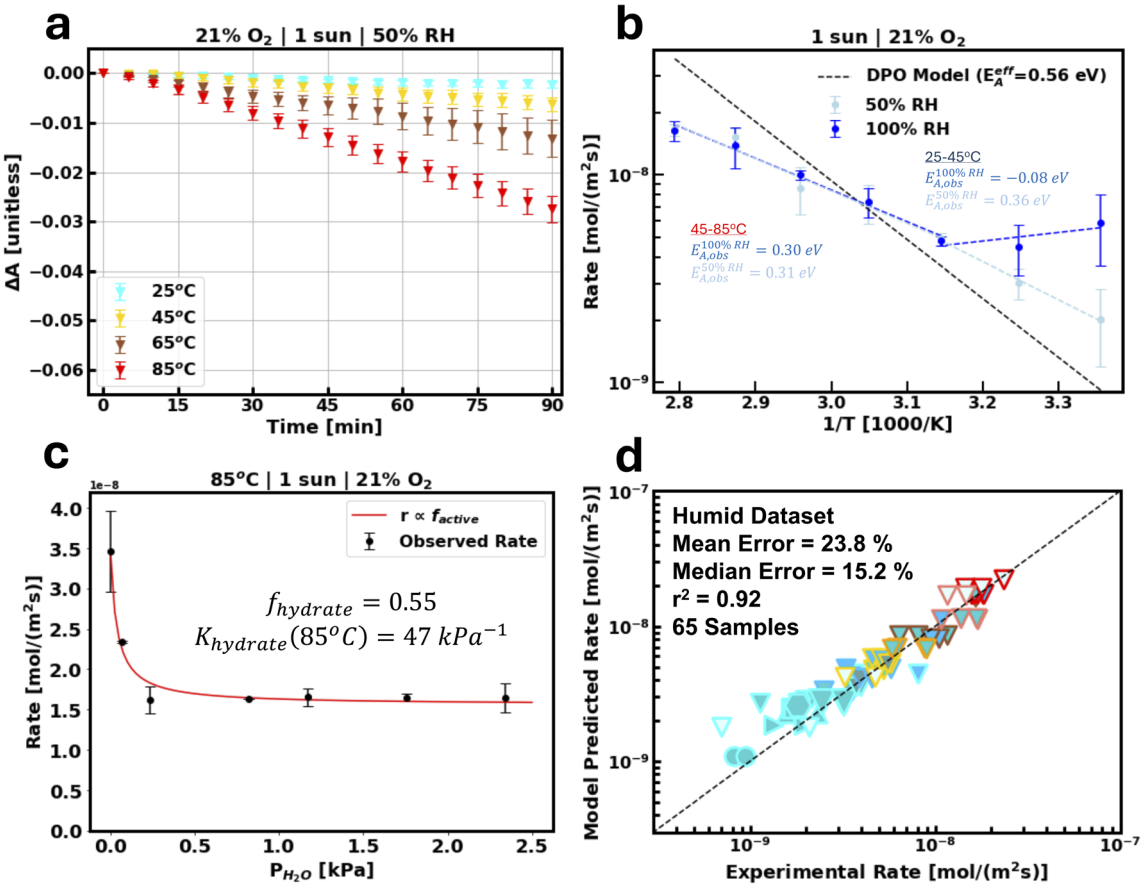

Fig. 3 Reaction kinetics for water-accelerated photooxidation and hydrate formation. (a) Change in absorbance over time for runs in 50% RH air, 1 sun at 25 °C, 45 °C, 65 °C, and 85 °C. (b) Arrhenius plot for runs in 50% and 100% RH compared to DPO model predicted rates. Apparent activation energies for low temperature (25–45 °C) and high temperature (45–85 °C) runs are shown. (c) Observed rate *versus* partial pressure of water vapor at 85 °C, 21% O_2, 1 sun illumination with model fit. (d) Parity plot for the humid dataset (65 total samples across a range of conditions with non-zero humidity, refer to Fig. 1 for symbol legend).

provides a strong fit to the data. We also find a relatively high activation energy associated with hydrate formation which indicates that this process has a large energy barrier to formation in this perovskite composition. As discussed in SI Section 8, $\Delta H^{\text{eff}}_{\text{hydrate}}$ is the sum of the enthalpy of adsorption for water vapor and the enthalpy of the hydrate formation reaction. For the humid dataset, we achieve an excellent fit of the data with a median error, mean error, and r^2 value of 15.2%, 23.8%, and 0.92, respectively (Fig. 3d). We have also included a bootstrap procedure (SI Section 9 and Fig. S8) identical to that done for the DPO parameters to estimate the uncertainty of the fitted WPO and HF parameters. The final WPO and HF parameter estimates and their uncertainties are included in Table 1. Expanded details for the fitting procedure for the water-accelerated photooxidation model and hydrate formation model are included in SI Section 9.

Conclusion

In conclusion, we identify two distinct oxygen and light-induced degradation pathways for $FA_{0.8}Cs_{0.2}Pb(I_{0.83}Br_{0.17})_3$ absorbers: (1) dry photooxidation ($E^{\text{eff}}_{\text{A,DPO}} = 0.56$ eV, with only superoxide radical as the oxidizing agent) and (2) water-accelerated photooxidation ($E^{\text{eff}}_{\text{A,WPO}} = -0.12$ eV, includes secondary ROSs as reactants). In addition, we demonstrate that water vapor retards decomposition at elevated temperatures in an oxygen containing environment, which is posited to be a result of hydrate formation that decreases the number of available surface adsorption sites for oxygen. A two-step reaction pathway for hydrate formation is used to derive an expression that accurately quantifies water's effect on total photooxidation rate. A complete rate expression for the chemical decomposition of this representative mixed-cation mixed-halide perovskite is reported and predicts the initial rate of degradation with low error (~14% median error for the total dataset of 120 runs across a range of oxygen and water partial pressures, photon fluxes, and temperatures, Fig. S10). This model is determined from degradation runs with greater than 3% ambient oxygen. However, in principle it provides an estimate at lower oxygen concentrations as well. It is, however, important to note that the unscavenged electrons at low O_2 partial pressures may react with Pb^{2+} to reduce it.[20,45,46] Our model should be accurate in quantifying the rate of perovskite loss due to reaction with superoxide and other ROSs but will miss the Pb^{2+} reduction

reaction at low O_2 partial pressure. To validate that the identified mechanisms are not unique to $FA_{0.8}Cs_{0.2}Pb(I_{0.83}Br_{0.17})_3$, we performed additional tests on $FA_{0.8}Cs_{0.2}Pb(I_{0.9}Br_{0.1})_3$ and $FA_{0.8}Cs_{0.2}PbI_3$ thin films (Fig. S11), which showed similar trends under combined oxygen, humidity, and illumination stresses. This model may also be useful in developing predictions of module lifetime when coupled with models of moisture and oxygen ingress through an encapsulant, as well as the effects of slower escape and build-up of gaseous decomposition products.

Conflicts of interest

There are no conflicts of interest to declare.

Data availability

Additional raw data and analysis scripts that support the findings of this work are available from the corresponding author upon reasonable request.

The majority of the data generated and analyzed in this work are included in this published article and the associated ESI. Supplementary information: Detailed experimental methods, probe beam wavelength selection data, comparison of photooxidation and oxidation, *ex situ* diffraction and absorption measurements during photooxidation, derivation of rate laws and bootstrap analysis for parameter fits, final modeling results for the complete dataset, and tests on two other compositions can be found in the supporting information. See DOI: **https://doi.org/10.1039/d5ta05228a**.

Acknowledgements

This material is based upon work supported by the U.S. Department of Energy's Office of Energy Efficiency and Renewable Energy (EERE) under Solar Energy Technology Office award number DE-EE0009351. This report was prepared as an account of work sponsored by an agency of the United States Government. Neither the United States Government nor any agency thereof, nor any of its employees, makes any warranty, express or implied, or assumes any legal liability or responsibility for the accuracy, completeness, or usefulness of any information, apparatus, product, or process disclosed, or represents that its use would not infringe privately owned rights. Reference herein to any specific commercial product, process, or service by trade name, trademark, manufacturer, or otherwise does not necessarily constitute or imply its endorsement, recommendation, or favoring by the United States Government or any agency thereof. The views and opinions of authors expressed herein do not necessarily state or reflect those of the United States Government or any agency thereof. The authors also acknowledge funding from the University of Washington Clean Energy Institute. Part of this work was conducted at the Molecular Analysis Facility, a National Nanotechnology Coordinated Infrastructure (NNCI) site at the University of Washington, which is supported in part by funds from the National Science Foundation (awards NNCI-2025489, NNCI-1542101).

References

1 T. D. Siegler, A. Dawson, P. Lobaccaro, D. Ung, M. E. Beck, G. Nilsen and L. L. Tinker, The Path to Perovskite Commercialization: A Perspective from the United States Solar Energy Technologies Office, *ACS Energy Lett.*, 2022, **7**(5), 1728–1734, DOI: **10.1021/acsenergylett.2c00698**.

2 T. Abzieher, D. T. Moore, M. Roß, S. Albrecht, J. Silvia, H. Tan, Q. Jeangros, C. Ballif, M. T. Hoerantner, B. S. Kim, H. J. Bolink, P. Pistor, J. C. Goldschmidt, Y. H. Chiang, S. D. Stranks, J. Borchert, M. D. McGehee, M. Morales-Masis, J. B. Patel, A. Bruno and U. W. Paetzold, Vapor Phase Deposition of Perovskite Photovoltaics: Short Track to Commercialization?, *Energy Environ. Sci.*, 2024, 1645–1663, DOI: **10.1039/d3ee03273f**.

3 Y. Vaynzof, The Future of Perovskite Photovoltaics—Thermal Evaporation or Solution Processing?, *Adv. Energy Mater.*, 2020, **10**(48), 2003073.

4 T. Leijtens, K. A. Bush, R. Prasanna and M. D. McGehee, Opportunities and Challenges for Tandem Solar Cells Using Metal Halide Perovskite Semiconductors, *Nat. Energy*, 2018, 828–838, DOI: **10.1038/s41560-018-0190-4**.

5 G. E. Eperon, S. D. Stranks, C. Menelaou, M. B. Johnston, L. M. Herz and H. J. Snaith, Formamidinium Lead Trihalide: A Broadly Tunable Perovskite for Efficient Planar Heterojunction Solar Cells, *Energy Environ. Sci.*, 2014, **7**(3), 982–988, DOI: **10.1039/c3ee43822h**.

6 S. Mahesh, J. M. Ball, R. D. J. Oliver, D. P. McMeekin, P. K. Nayak, M. B. Johnston and H. J. Snaith, Revealing the Origin of Voltage Loss in Mixed-Halide Perovskite Solar Cells, *Energy Environ. Sci.*, 2020, **13**(1), 258–267, DOI: **10.1039/c9ee02162k**.

7 A. J. Knight and L. M. Herz, Preventing Phase Segregation in Mixed-Halide Perovskites: A Perspective, *Energy Environ. Sci.*, 2020, 2024–2046, DOI: **10.1039/d0ee00788a**.

8 E. T. Hoke, D. J. Slotcavage, E. R. Dohner, A. R. Bowring, H. I. Karunadasa and M. D. McGehee, Reversible Photo-Induced Trap Formation in Mixed-Halide Hybrid Perovskites for Photovoltaics, *Chem. Sci.*, 2015, **6**(1), 613–617, DOI: **10.1039/c4sc03141e**.

9 E. Köhnen, M. Jošt, A. B. Morales-Vilches, P. Tockhorn, A. Al-Ashouri, B. Macco, L. Kegelmann, L. Korte, B. Rech, R. Schlatmann, B. Stannowski and S. Albrecht, Highly Efficient Monolithic Perovskite Silicon Tandem Solar Cells: Analyzing the Influence of Current Mismatch on Device Performance, *Sustain. Energy Fuels*, 2019, **3**(8), 1995–2005, DOI: **10.1039/c9se00120d**.

10 W. Tan, A. R. Bowring, A. C. Meng, M. D. McGehee and P. C. McIntyre, Thermal Stability of Mixed Cation Metal Halide Perovskites in Air, *ACS Appl. Mater. Interfaces*, 2018, **10**(6), 5485–5491, DOI: **10.1021/acsami.7b15263**.

11 V. L. Pool, B. Dou, D. G. Van Campen, T. R. Klein-Stockert, F. S. Barnes, S. E. Shaheen, M. I. Ahmad, M. F. A. M. Van Hest and M. F. Toney, Thermal Engineering of FAPbI3 Perovskite Material via Radiative Thermal Annealing and In situ XRD, *Nat. Commun.*, 2017, **8**, 14075.

12 A. Donakowski, D. W. Miller, N. C. Anderson, A. Ruth, E. M. Sanehira, J. J. Berry, M. D. Irwin, A. Rockett and K. X. Steirer, Improving Photostability of Cesium-Doped Formamidinium Lead Triiodide Perovskite, *ACS Energy Lett.*, 2021, **6**(2), 574–580, DOI: 10.1021/acsenergylett.0c02339.

13 M. De Keersmaecker, P. Dietrich, M. Bahri, N. D. Browning, N. R. Armstrong and E. L. Ratcliff, Activated Corrosion and Recovery in Lead Mixed-Halide Perovskites Revealed by Dynamic Near-Ambient Pressure X-Ray Photoelectron Spectroscopy, *J. Am. Chem. Soc.*, 2025, **147**, 88881–88892.

14 Z. Chen, Z. Yang, S. Du, D. Lin, F. Zhang, Y. Zeng, G. Liu, Z. Nie and L. Ma, Thermal Stability and Decomposition Kinetics of Mixed-Cation Halide Perovskites, *Phys. Chem. Chem. Phys.*, 2023, **25**(48), 32966–32971, DOI: 10.1039/d3cp03704e.

15 T. D. Siegler, W. A. Dunlap-Shohl, Y. Meng, Y. Yang, W. F. Kau, P. P. Sunkari, C. E. Tsai, Z. J. Armstrong, Y. C. Chen, D. A. C. Beck, M. Meilă and H. W. Hillhouse, Water-Accelerated Photooxidation of CH3NH3PbI3 Perovskite, *J. Am. Chem. Soc.*, 2022, **144**(12), 5552–5561, DOI: 10.1021/jacs.2c00391.

16 Y. Meng, P. P. Sunkari, M. Meilă and H. W. Hillhouse, Chemical Reaction Kinetics of the Decomposition of Low-Bandgap Tin-Lead Halide Perovskite Films and the Effect on the Ambipolar Diffusion Length, *ACS Energy Lett.*, 2023, **8**(4), 1688–1696, DOI: 10.1021/acsenergylett.2c02733.

17 R. J. Stoddard, W. A. Dunlap-Shohl, H. Qiao, Y. Meng, W. F. Kau and H. W. Hillhouse, Forecasting the Decay of Hybrid Perovskite Performance Using Optical Transmittance or Reflected Dark-Field Imaging, *ACS Energy Lett.*, 2020, **5**(3), 946–954, DOI: 10.1021/acsenergylett.0c00164.

18 W. A. Dunlap-Shohl, Y. Meng, P. P. Sunkari, D. A. C. Beck, M. Meilă and H. W. Hillhouse, Physiochemical Machine Learning Models Predict Operational Lifetimes of $CH_3NH_3PbI_3$ Perovskite Solar Cells, *J. Mater. Chem. A*, 2024, **12**(16), 9730–9746, DOI: 10.1039/D3TA06668A.

19 I. L. Repins, M. Owen-Bellini, M. D. Kempe, M. G. Deceglie, J. J. Berry, N. Y. Doumon, T. J. Silverman and L. T. Schelhas, Interpreting Accelerated Tests on Perovskite Modules Using Photooxidation of MAPbI3 as an Example, *Cell Rep. Phys. Sci.*, 2024, **5**(5), 101969, DOI: 10.1016/j.xcrp.2024.101969.

20 S. G. Cira, W. A. Dunlap-Shohl, Y. Meng, P. P. Sunkari, J. H. Folch and H. W. Hillhouse, Light-Induced Degradation of Mixed-Cation, Mixed-Halide Perovskite: Observed Rates and Influence of Oxygen, *J. Mater. Chem. A*, 2025, **13**(7), 5033–5044, DOI: 10.1039/D4TA07807A.

21 N. Aristidou, C. Eames, I. Sanchez-Molina, X. Bu, J. Kosco, M. Saiful Islam and S. A. Haque, Fast Oxygen Diffusion and Iodide Defects Mediate Oxygen-Induced Degradation of Perovskite Solar Cells, *Nat. Commun.*, 2017, **8**, 15218.

22 Y. Ju, X. Hu, X. g. Wu, C. Wang, A. Baranov, A. Pushkarev and H. Zhong, The Interactions between Halide Perovskites and Oxygen: From Stages to Strategies, *Matter*, 2024, 3756–3785, DOI: 10.1016/j.matt.2024.08.007.

23 N. Aristidou, I. Sanchez-Molina, T. Chotchuangchutchaval, M. Brown, L. Martinez, T. Rath and S. A. Haque, The Role of Oxygen in the Degradation of Methylammonium Lead Trihalide Perovskite Photoactive Layers, *Angew. Chem.*, 2015, **127**(28), 8326–8330, DOI: 10.1002/ange.201503153.

24 J. Hidalgo, W. Kaiser, Y. An, R. Li, Z. Oh, A. F. Castro-Méndez, D. K. LaFollette, S. Kim, B. Lai, J. Breternitz, S. Schorr, C. A. R. Perini, E. Mosconi, F. De Angelis and J. P. Correa-Baena, Synergistic Role of Water and Oxygen Leads to Degradation in Formamidinium-Based Halide Perovskites, *J. Am. Chem. Soc.*, 2023, **145**, 24549–24557.

25 P. Raval, M. A. Akhavan Kazemi, J. Ruellou, J. Trébosc, O. Lafon, L. Delevoye, F. Sauvage and G. N. Manjunatha Reddy, Examining a Year-Long Chemical Degradation Process and Reaction Kinetics in Pristine and Defect-Passivated Lead Halide Perovskites, *Chem. Mater.*, 2023, **35**(7), 2904–2917, DOI: 10.1021/acs.chemmater.2c03803.

26 H. S. Kim, C. R. Lee, J. H. Im, K. B. Lee, T. Moehl, A. Marchioro, S. J. Moon, R. Humphry-Baker, J. H. Yum, J. E. Moser, M. Grätzel and N. G. Park, Lead Iodide Perovskite Sensitized All-Solid-State Submicron Thin Film Mesoscopic Solar Cell with Efficiency Exceeding 9%, *Sci. Rep.*, 2012, **2**, 591.

27 Y. Ouyang, Y. Li, P. Zhu, Q. Li, Y. Gao, J. Tong, L. Shi, Q. Zhou, C. Ling, Q. Chen, Z. Deng, H. Tan, W. Deng and J. Wang, Photo-Oxidative Degradation of Methylammonium Lead Iodide Perovskite: Mechanism and Protection, *J. Mater. Chem. A*, 2019, **7**(5), 2275–2282, DOI: 10.1039/c8ta12193a.

28 D. Bryant, N. Aristidou, S. Pont, I. Sanchez-Molina, T. Chotchunangatchaval, S. Wheeler, J. R. Durrant and S. A. Haque, Light and Oxygen Induced Degradation Limits the Operational Stability of Methylammonium Lead Triiodide Perovskite Solar Cells, *Energy Environ. Sci.*, 2016, **9**(5), 1655–1660, DOI: 10.1039/c6ee00409a.

29 Q. Sun, P. Fassl, D. Becker-Koch, A. Bausch, B. Rivkin, S. Bai, P. E. Hopkinson, H. J. Snaith and Y. Vaynzof, Role of Microstructure in Oxygen Induced Photodegradation of Methylammonium Lead Triiodide Perovskite Films, *Adv. Energy Mater.*, 2017, **7**(20), 1700977.

30 E. J. Juarez-Perez, L. K. Ono and Y. Qi, Thermal Degradation of Formamidinium Based Lead Halide Perovskites into: Sym -Triazine and Hydrogen Cyanide Observed by Coupled Thermogravimetry-Mass Spectrometry Analysis, *J. Mater. Chem. A*, 2019, **7**(28), 16912–16919, DOI: 10.1039/c9ta06058h.

31 T. Webb and S. A. Haque, A Comparison of Molecular Iodine Evolution on the Chemistry of Lead and Tin Perovskites, *Energy Environ. Sci.*, 2024, 3244–3269, DOI: 10.1039/d3ee03004k.

32 S. Kotz and N. L. Johnson, *Breakthroughs in Statistics: Methodology and Distribution*, Springer, New York, 1992.

33 L. Zhang and P. H. L. Sit, Ab Initio Study of Interaction of Water, Hydroxyl Radicals, and Hydroxide Ions with CH3NH3PbI3 and CH3NH3PbBr3 Surfaces, *J. Phys. Chem. C*, 2015, **119**(39), 22370–22378, DOI: 10.1021/acs.jpcc.5b07000.

34 L. Zhang and P. H. L. Sit, Ab Initio Static and Dynamic Study of CH3NH3PbI3 Degradation in the Presence of Water, Hydroxyl Radicals, and Hydroxide Ions, *RSC Adv.*, 2016, **6**(80), 76938–76947, DOI: **10.1039/c6ra12781a**.

35 G. R. McAndrews, B. Guo, S. C. Kaczaral, K. Fukuda, M. R. S. Poma, R. A. Belisle, A. Amassian and M. D. McGehee, Moisture Uptake Relaxes Stress in Metal Halide Perovskites at the Expense of Stability, *ACS Energy Lett.*, 2024, **9**(8), 4153–4161, DOI: **10.1021/acsenergylett.4c01817**.

36 D.-H. Chin, G. Chiericato, E. J. Nanni and D. T. Sawyer, Proton-Induced Disproportionation of Superoxide Ion in Aprotic Media, *J. Am. Chem. Soc.*, 1982, **104**(104), 1296–1299.

37 A. M. A. Leguy, Y. Hu, M. Campoy-Quiles, M. I. Alonso, O. J. Weber, P. Azarhoosh, M. Van Schilfgaarde, M. T. Weller, T. Bein, J. Nelson, P. Docampo and P. R. F. Barnes, Reversible Hydration of CH3NH3PbI3 in Films, Single Crystals, and Solar Cells, *Chem. Mater.*, 2015, **27**(9), 3397–3407, DOI: **10.1021/acs.chemmater.5b00660**.

38 Z. Zhu, V. G. Hadjiev, Y. Rong, R. Guo, B. Cao, Z. Tang, F. Qin, Y. Li, Y. Wang, F. Hao, S. Venkatesan, W. Li, S. Baldelli, A. M. Guloy, H. Fang, Y. Hu, Y. Yao, Z. Wang and J. Bao, Interaction of Organic Cation with Water Molecule in Perovskite MAPbI3: From Dynamic Orientational Disorder to Hydrogen Bonding, *Chem. Mater.*, 2016, **28**(20), 7385–7393, DOI: **10.1021/acs.chemmater.6b02883**.

39 J. Cao, X. Zhang, Y. Miao, W. Li, X. Zeng, S. Yang, C. Yan, J. Lu and W. Yang, Interactions between H2O and Lead Halide Perovskites: Recent Progress and Applications, *Matter*, 2024, 3728–3755, DOI: **10.1016/j.matt.2024.08.001**.

40 L. Hu, G. Shao, T. Jiang, D. Li, X. Lv, H. Wang, X. Liu, H. Song, J. Tang and H. Liu, Investigation of the Interaction between Perovskite Films with Moisture via in Situ Electrical Resistance Measurement, *ACS Appl. Mater. Interfaces*, 2015, **7**(45), 25113–25120, DOI: **10.1021/acsami.5b06268**.

41 J. Yang, B. D. Siempelkamp, D. Liu and T. L. Kelly, Investigation of CH3NH3PbI3 degradation Rates and Mechanisms in Controlled Humidity Environments Using In situ Techniques, *ACS Nano*, 2015, **9**(2), 1955–1963, DOI: **10.1021/nn506864k**.

42 L. Zhang, M. G. Ju and W. Liang, The Effect of Moisture on the Structures and Properties of Lead Halide Perovskites: A First-Principles Theoretical Investigation, *Phys. Chem. Chem. Phys.*, 2016, **18**(33), 23174–23183, DOI: **10.1039/c6cp01994c**.

43 C. Ma, F. T. Eickemeyer, S.-H. Lee, D.-H. Kang, S. J. Kwon, M. Grätzel and N.-G. Park, Unveiling Facet-Dependent Degradation and Facet Engineering for Stable Perovskite Solar Cells, *Science*, 2023, **379**, 173–178**https://www.science.org**.

44 T. Hastie, R. Tibshirani and J. Friedman, *The Elements of Statistical Learning: Data Mining, Inference, and Prediction*, Springer, New York, 2017.

45 J. Hieulle, A. Krishna, A. Boziki, J. N. Audinot, M. U. Farooq, J. F. Machado, M. Mladenović, H. Phirke, A. Singh, T. Wirtz, A. Tkatchenko, M. Graetzel, A. Hagfeldt and A. Redinger, Understanding and Decoupling the Role of Wavelength and Defects in Light-Induced Degradation of Metal-Halide Perovskites, *Energy Environ. Sci.*, 2023, **17**(1), 284–295, DOI: **10.1039/d3ee03511e**.

46 S. Macpherson, T. A. S. Doherty, A. J. Winchester, S. Kosar, D. N. Johnstone, Y. H. Chiang, K. Galkowski, M. Anaya, K. Frohna, A. N. Iqbal, S. Nagane, B. Roose, Z. Andaji-Garmaroudi, K. W. P. Orr, J. E. Parker, P. A. Midgley, K. M. Dani and S. D. Stranks, Local Nanoscale Phase Impurities Are Degradation Sites in Halide Perovskites, *Nature*, 2022, **607**(7918), 294–300, DOI: **10.1038/s41586-022-04872-1**.